2017 IEEE International Conference on Robotics and Automation (ICRA)
Singapore, May 29 - June 3, 2017

A High-Force, High-Stroke Distal Robotic Add-On for Endoscopy*

Joshua B. Gafford, *Student Member, IEEE,* Robert J. Wood, *Senior Member, IEEE,* and Conor J. Walsh, *Member, IEEE*

***Abstract*—'Snap-On' robotic modules that can integrate distally with existing commercially-available endoscopic equipment have the potential to provide new capabilities such as enhanced dexterity, bilateral manipulation and feedback sensing with minimal disruption of the current clinical workflow. However, the desire for fully-distal integration of sensors and actuators and the resulting form factor requirements preclude the use of many off-the-shelf actuators capable of generating the relevant strokes and forces required to interact with tools and tissue. In this work, we investigate the use of millimeter-scale, optimally-packed helical shape memory alloy (SMA) actuators in an antagonistic configuration to provide distal actuation without the need for a continuous mechanical coupling to proximal, off-board actuation packages to realize a truly plug-and-play solution. Using phenomenological modeling, we design and fabricate antagonistic helical SMA pairs and implement them in an at-scale roboendoscopic module to generate strokes and forces necessary for deflecting tools passed through the endoscope working port, thereby providing a controllable robotic 'wrist' inside the body to otherwise passive flexible tools. Bandwidth is drastically improved through the integration of targeted fluid cooling. The integrated system can generate maximum lateral forces of 10N and demonstrates an additional 96 degrees of distal angulation, expanding the reachable workspace of tools passed through a standard endoscope.**

I. INTRODUCTION

ENDOSCOPE-based systems enable intraluminal access to confined anatomy through natural orifices, resulting in both cosmetic and economic benefits over more invasive procedures [1]. While there is growing interest in performing complex therapeutic procedures endoscopically, such as endoscopic submucosal dissection (ESD), endoscope technology itself has remained relatively unchanged for several decades, and as a result, widespread applications thereof are primarily diagnostic in nature. There is a real incentive to innovate in the field and close the gap between the state of the technology and the demand for more complex minimally-invasive procedures.

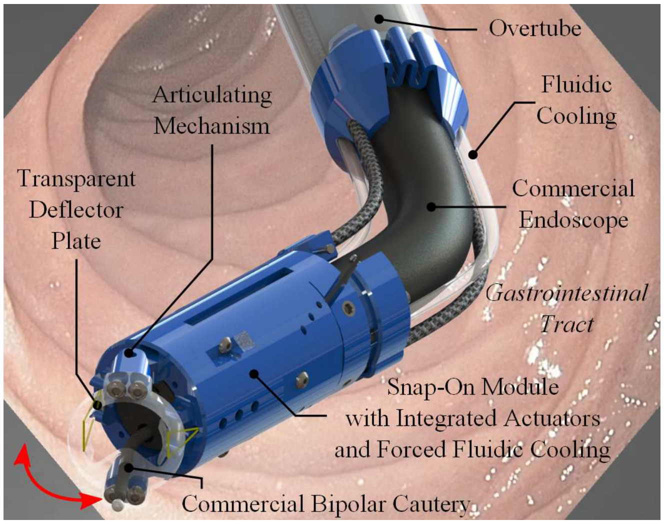

Fig. 1. Conceptual rendering of snap-on robotic module integrated onto a commercial endoscope, providing an additional yaw degree-of-freedom for precise control of cutting tools passed through the working channel.

A. Prior Work

Robotic endoscopy is a rich academic field encompassing a number of areas, including but not limited to teleoperation using novel actuation systems, haptic sensing, novel actuation technologies, rapid manufacturing of highly-articulate continuum structures, capsular approaches, and the design and control of dexterous robotic end-effectors [2]–[8]. Commercially, companies like Auris Robotics, Medrobotics and Invendo Medical are beginning to spin out these technologies into commercial products that promise greater access to and visualization of anatomy through natural orifices.

A characteristic common among numerous endoscopic robots presented in literature is the intimate mechanical coupling between distal end-effectors and proximal actuator systems. Typically this coupling is achieved via tendon-sheath systems (TSS). This approach has resulted in significant innovation in the field of flexible surgical robotics, granting endoscopists with unprecedented dexterity *in vivo*. The requirement for flexibility can result in hysteretic and nonlinear behaviors arising from tendon compliance, friction, and capstan effects resulting from sheath curvature. These

---

*This material based on work supported by Defense Advanced Research Projects Agency (DARPA), A2P (Grant No. FA8650-15-C-7548). This work was also partially funded by the Wyss Institute for Biologically Inspired Engineering and the John A. Paulson School of Engineering and Applied Sciences at Harvard University.

J. Gafford (corresponding author) is with the John A. Paulson School of Engineering and Applied Sciences at Harvard University, Cambridge, MA 02138 USA (jgafford@seas.harvard.edu).

R. Wood and C. Walsh are with the Faculty of the John A. Paulson School of Engineering and Applied Sciences at Harvard University, Cambridge, MA 02138 USA, and the Wyss Institute for Biologically-Inspired Engineering, Harvard University, Boston, MA 02115 USA (rwood, walsh@seas.harvard.edu).

effects make such systems difficult to model and control. In addition, proximal actuator packages that drive these systems can be large, cumbersome and potentially occlusive to the surgical arena, thereby requiring alterations to the clinical workflow to allow for docking/registration and undocking of these systems.

Due to fundamental limitations in manufacturing of mm-scale electromechanical systems and the dearth of commercially-available sensing and actuation options that conform to the strict form factor and robustness requirements, very few groups have focused on developing affordable, distal robotic modules with fully-integrated sensors and actuators [9]. We are working to develop robotic systems with sensors and actuators located entirely at the distal end to remove the mechanical coupling and realize a truly modular and deployable system. This work leverages prior work in design and monolithic fabrication of mechanisms, sensors and actuators at the mm-scale [10]–[12].

B. Contribution

Deployable endoscopic robotic systems, as shown in Fig. 1, preclude the use of conventional actuators (DC motors, voice coils, etc.) due to size limitations and the desire to remove the mechanical coupling between distal and proximal ends. As such, with the goal of 'moving everything to the tip,' we consider alternative actuation strategies that are acquiescent to the rigorous form factor requirements of fully-distal implementations. One such strategy employs the use of energy-dense phase changing materials (shape memory alloys, or SMAs) to provide low-to-moderate actuation speed and high force for actuating distal structures. In our previous work [10] we have shown that wire-based SMA actuators can be used for distal actuation of an articulating structure. However, the low strain capabilities (4-5%) ultimately limited the dexterity we were able to demonstrate.

To enable greater dexterity while matching (or exceeding) force output capabilities of previous designs, we require higher-stroke actuation systems capable of generating a high net lateral force to deflect common flexible endoscopic tools. To this end, we explore the use of helical SMA actuators. With the objective functions of (a) minimizing the overall form-factor (spring diameter and length) while (b) maximizing the force and stroke, the problem can be naturally posed as an optimization of work per unit volume. However, given the difficulties associated with accurately modeling helical SMA actuators, it can be deceitful to rely on model-based techniques alone to find a local optimum. As such, we implement an approach that combines approximate phenomenological modeling and experimental validation to converge on and identify a configuration that meets functional requirements. After discovering an optimized configuration, we implement the actuators in an at-scale robotic module and demonstrate greatly improved stroke characteristics.

In *Section II* we present a fixed-strain constitutive model used to approximate the blocking force evolution, as well as a quasi-steady version of the full phenomenological antagonism model for predicting net force vs. strain. In *Section III* we discuss the fabrication and control of helical SMA antagonistic pairs per model requirements. In *Section IV* we present experimental results of the optimized actuator design and validate both models. *Section V* discusses the integration of the actuators into an at-scale roboendoscopic module analog and preliminary results thereof.

II. SMA MODELING AND FABRICATION

Several SMA-based flexible robotic systems with medical applications have been demonstrated in literature [13], [14]. However, these systems typically suffer from limited force generation [15], limited stroke [16], or prohibitively slow actuation speeds [17]. In this work, we aim to generate high-force, high-stroke actuation at practical speeds through heuristic design of optimum actuator configurations coupled with the integration of forced fluidic cooling.

A. Fixed-Strain Model for Blocking Force

Modeling the blocking force of helical SMA actuators involves solving the quasi-steady, fixed strain form of the shear-based constitutive equation [18], [19]:

$$\tau - \tau_0 = G_\tau \cancelto{0}{(\gamma - \gamma_0)} + \Omega_S(\xi_S - \xi_{S0}) + \Theta(T - T_0) \quad (1)$$

where τ, τ_0 is instantaneous/initial shear stress, γ, γ_0 is the instantaneous/initial shear strain, ξ_S, ξ_{S0} is the instantaneous/initial martensitic fraction, T, T_0 is the instantaneous/initial temperature, G_τ is the shear modulus, Θ is the thermal expansion factor, and Ω_S is the stress-induced phase transformation contribution factor (which can be expressed as $\Omega_S = -\gamma_L G_\tau$ where γ_L is the maximum residual strain) [20]. Note that, for blocking force (fixed strain), the first term cancels out of Equation (1). Using the dual-phase model ($\xi = \xi_S + \xi_T$ is the sum of the shear- and temperature-dependent martensitic fractions), the shear modulus is phase-dependent:

$$G_\tau = G_a + \xi(G_m - G_a) \quad (2)$$

where G_m and G_a are the shear moduli in the martensitic and austenitic phases, respectively. The instantaneous martensitic phase components are dependent on initial conditions and the overall phase fraction as follows:

$$\xi_S = \xi_{S0} - \frac{\xi_{S0}}{\xi_0}(\xi_0 - \xi) \quad (3)$$

$$\xi_T = \xi_{T0} - \frac{\xi_{T0}}{\xi_0}(\xi_0 - \xi) \quad (4)$$

The phase kinetics can be described by a cosine model proposed by [18], where the total martensitic fraction for the reverse transformation (martensite to austenite) is given by:

$$\xi(T, \tau) = \frac{\xi_0}{2}\left[\cos\left(a_A\left(T - A_s - \frac{\sqrt{3}|\tau|}{C_A}\right)\right) + 1\right] \quad (5)$$

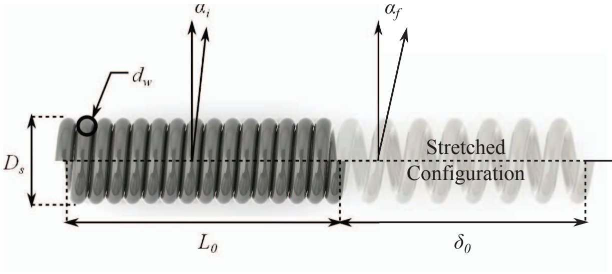

Fig. 2. Schematic of a helical actuator and relevant geometric parameters.

where ξ_0 is the initial martensite fraction ($\xi_0 = 1$), and $a_A = \frac{\pi}{A_s - A_f}$ where A_s and A_f are the austenite start and finish temperatures respectively, and C_A is a curve-fit parameter.

In anticipation of current-based control, we describe the temperature dynamics using a simple convective heat transfer model modified to include the effects of Joule heating due to an applied current (note: this assumes that there are no thermal gradients, radial or axial, within the wire):

$$mC_p\dot{T} = I^2R - h_cA_c(T - T_\infty) \tag{6}$$

where m is the mass of the actuator, C_p is the specific heat, I is the applied current, R is the actuator's electrical resistance, h_c is the convective heat transfer coefficient, A_c is the actuator's surface area, and T_∞ is the ambient temperature. Finally, from a geometric perspective, we can transform initial pre-stretch δ_0 into shear strain $\gamma_0 = \gamma(\delta_0)$ via the following [21]:

$$\gamma(\delta_0) = \frac{3d_w}{4D_s}\cos(\alpha_0)\left(\sin(\alpha_f(\delta_0) - \sin(\alpha_i))\right) \tag{7}$$

where relevant geometric parameters are given in Fig. 2, and initial and final pitch angles α_i and α_f are expressed as:

$$\alpha_i = \tan^{-1}\left(\frac{d_w}{\frac{1}{2}D_s}\right) \tag{8}$$

$$\alpha_f(\delta_0) = \sin^{-1}\left(\frac{\delta_0\cos\alpha_i}{\pi N D_s} + \sin\alpha_i\right) \tag{9}$$

A blocking force analysis requires the following set of initial conditions: $\{T_\infty, \tau_0, \xi_{S0}\,\gamma_0\}$. A pre-stretch $\delta_0 \to \gamma_0$ while in the fully martensitic state will result in induced shear stress τ_0 and, depending on the amount of stress, some initial martensitic detwinning ξ_{S0}. We note that, although temperature T can be solved for explicitly, equations relating shear stress τ, stress-induced phase volume ξ_S, and temperature T are transcendentally related, requiring the use of gradient-based techniques to solve for the stress and phase kinetics for a given temperature. An alternative, more computationally tractable approach is to exploit the slow phase dynamics and solve for the equations in discrete time by 'updating' the phase and stress at each point along the temperature profile, and initializing the process by solving for some initial configuration $\tau_0 = G_m\gamma_0 - \gamma_L G_m\xi_{S0} + \Theta T_\infty$ and $\xi_{S0} = \xi(T_\infty, \tau_0)$ simultaneously using gradient descent or a nonlinear solver. As a heat profile is applied, we can evolve the stress-based phase kinetics in discrete time according to the following transition law:

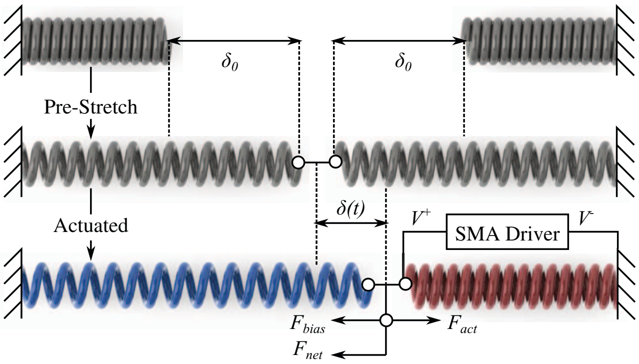

Fig. 3. Schematic of antagonistic actuation and force balance.

$$\xi_S^{(n+1)} = \begin{cases} \xi(T^{(n)}, \tau^{(n)}) & \text{if } A_s' < T^{(n)} < A_f' \\ \xi_S^{(n)} & \text{otherwise} \end{cases} \tag{10}$$

where $A_s' = (A_s + \frac{\sqrt{3}\tau^{(n)}}{C_A})$ is the stress-modified austenitic start temperature and $A_f' = (A_f + \frac{\sqrt{3}\tau^{(n)}}{C_A})$ is the stress-modified austenitic final temperature. The shear modulus and stress are subsequently updated:

$$G_\tau^{(n+1)} = G_a + \xi(T^{(n)}, \tau^{(n)})(G_m - G_a) \tag{11}$$

$$\tau^{(n+1)} = -\gamma_L G_\tau^{(n+1)}\left(\xi_S^{(n+1)} - \xi_{S0}\right) + \Theta\left(T^{(n)} - T_\infty\right) + \tau_0 \tag{12}$$

We can update the blocking force:

$$\begin{aligned} F^{(n+1)} &= K(G_\tau^{(n+1)}, \alpha_f(\delta_0))\delta_0 \\ &\quad - \frac{\pi d_w^3}{8D_s}G_\tau^{(n+1)}\gamma_L\left(\xi_S^{(n+1)} - \xi_{S0}\right) \end{aligned} \tag{13}$$

Note that in the above equation there is also the nonlinear effect of martensitic detwinning (which can be ignored when considering a fully-transformed actuator). We define an effective linear-elastic stiffness K as [21]:

$$K(G_{(\cdot)}, \alpha) = \frac{G_{(\cdot)}d_w^4}{8D_s^3N}\left(\frac{\cos^3\alpha_i}{\cos^2\alpha(\cos^2\alpha + \sin^2\alpha/(1+\nu))}\right) \tag{14}$$

where ν is the Poisson ratio of the material.

B. Modeling Antagonism

If we wish to model antagonistic behavior with strain dynamics, as shown in Fig 3, the model becomes more complicated as we can no longer ignore the first term on the right side in Equation (1). In this case we assume that the active actuator is biased by a (geometrically identical) passive actuator in martensitic state where the martensitic de-twinning phenomena are stress-dominated and can be described by the cosine model:

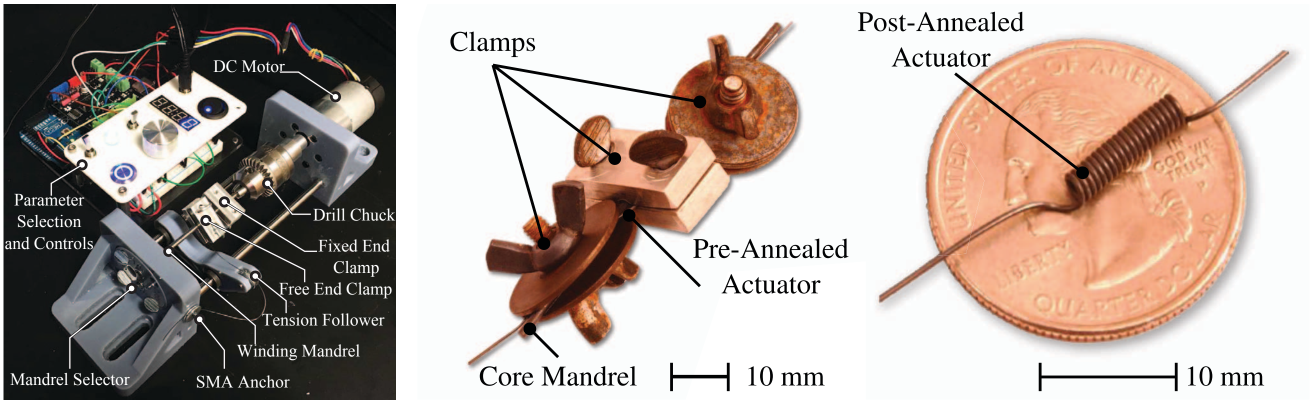

(a)

(b)

Fig. 4. *(a)* Setup for winding and shape-setting helical SMA actuators, *(b)* actuator in different stages of fabrication process, where *(left)* shows the constrained actuator prior to annealing, and *(right)* shows the resulting actuator post-annealing.

$$\xi_{Sb} = \frac{1-\xi_{Sb0}}{2}\cos\left[\frac{\pi}{\tau_s^{cr}-\tau_f^{cr}}(\tau_b-\tau_f^{cr})\right]+\frac{1+\xi_{Sb0}}{2} \tag{15}$$

where τ_s^{cr} and τ_f^{cr} are the critical shear stresses at the start and finish of the conversion, respectively, and τ_b is the shear stress in the martensitic state. Note that we introduce subscript b to differentiate the bias spring dynamics from those of the active spring.

As before, we have the following discrete-time update law for the phase kinetics describing the detwinned martensite volume fraction:

$$\xi_{Sb}^{(n+1)} = \begin{cases} \text{Equation (15)} & \text{if } \tau_s^{cr} < \tau_b^{(n)} < \tau_f^{cr} \\ \xi_{Sb}^{(n)} & \text{otherwise} \end{cases} \tag{16}$$

In contrast to the blocking force model, the strain rate is no longer negligible, and is a function of the system kinematics. Here we assume that the strain rate in the active actuator is dictated by the elastic compliance of the bias element and some net blocking force (which we assume is constant), and we also assume steady-state thermodynamics within the bias element. Casting into discrete time and using a simple force balance shown in Fig. 3, given some instantaneous deflection $\Delta^{(n+1)}$, we can write $F_b^{(n+1)}$ and $F_a^{(n+1)}$ as:

$$\begin{aligned} F_b^{(n+1)} &= K\left(G_m, \alpha_f(\delta_0+\Delta^{(n+1)})\right)\left[\delta_0+\Delta^{(n+1)}\right] \\ &\quad - \frac{\pi d_w^3}{8D_s} G_m \gamma_L(\xi_{Sb}^{(n+1)}-\xi_{Sb0}) \\ &= F_a^{(n+1)} - F_{net} \end{aligned} \tag{17}$$

$$\begin{aligned} F_a^{(n+1)} &= K\left(G_\tau^{(n+1)}, \alpha_f(\delta_0-\Delta^{(n+1)})\right)\left[\delta_0-\Delta^{(n+1)}\right] \\ &\quad - \frac{\pi d_w^3}{8D_s} G_\tau^{(n+1)} \gamma_L(\xi_{Sa}^{(n+1)}-\xi_{Sa0}) \end{aligned} \tag{18}$$

We re-iterate that the phase characteristics in the active actuator have contributions from both detwinned martensite and austenite during the heating cycle, whereas the bias actuator phase is characterized by the former only.

We can solve Equations (17) and (18) for $\Delta^{(n+1)}$ using gradient-based techniques to solve for deflection as a function of time given a known input current profile. Alternatively, a much simpler analysis is to prescribe a known set of Δ and set $G_\tau \to G_a$ and $\xi_{Sa} \to 0$ in Equation (18) (i.e. putting the active actuator in a fully austenitic state) to observe the force margin (i.e. $F_a - F_b$) as a function of stroke. This is the approach we implemented later in *Section IV* when comparing the model with experimental results. Regardless of the approach, the shear strains in the active and bias actuators are updated accordingly: $\gamma_a^{(n+1)} = \gamma(\delta_0 - \Delta^{(n+1)})$, $\gamma_b^{(n+1)} = \gamma(\delta_0 + \Delta^{(n+1)})$. Shear stresses and moduli are incremented as in the previous section for both the active and bias actuator, but with the addition of the strain term.

III. FABRICATION AND CONTROL

A. *Fabrication*

Custom helical actuators were fabricated in-house using the setup shown in Fig. 4(a). The setup allows for flexible fabrication over a wide parameter space, accomodating a range of different wire diameters and core sizes. A tension following system ensures optimal packing (pitch = d_w). Fig. 4(b) shows the actuator both in the shape-setting clamps *(left)*, and after annealing at 400C for 1 hour *(right)*.

B. *Electronics and Control*

1) Power/Sensing Electronics: Custom power/sensing electronics, shown in Fig. 5, were designed and fabricated to enable digital control of the current in two actuators simultaneously via pulse-width modulation (PWM). PWM control was selected due to ease of digital implementation as the inherent low-pass of SMA thermomechanics filters the high-frequency PWM to simulate an analog current control signal. A square wave with varying duty cycle drives the gate of a power NPN MOSFET which sinks current through the SMA, a variable ceramic power resistor that serves as a current limiter, and whatever series resistance arises

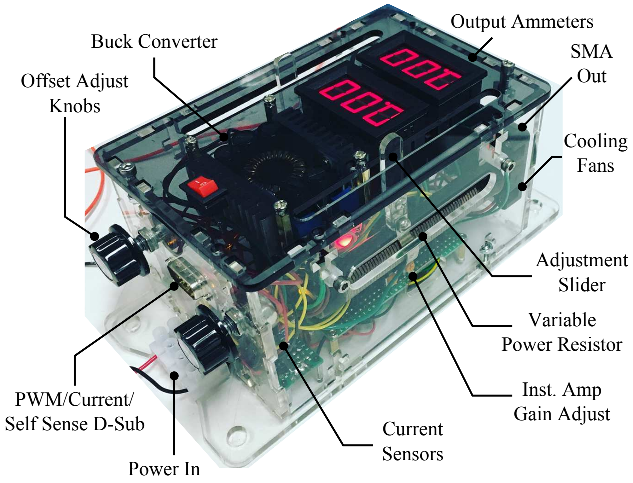

Fig. 5. Fabricated power/sensing electronics and custom enclosure.

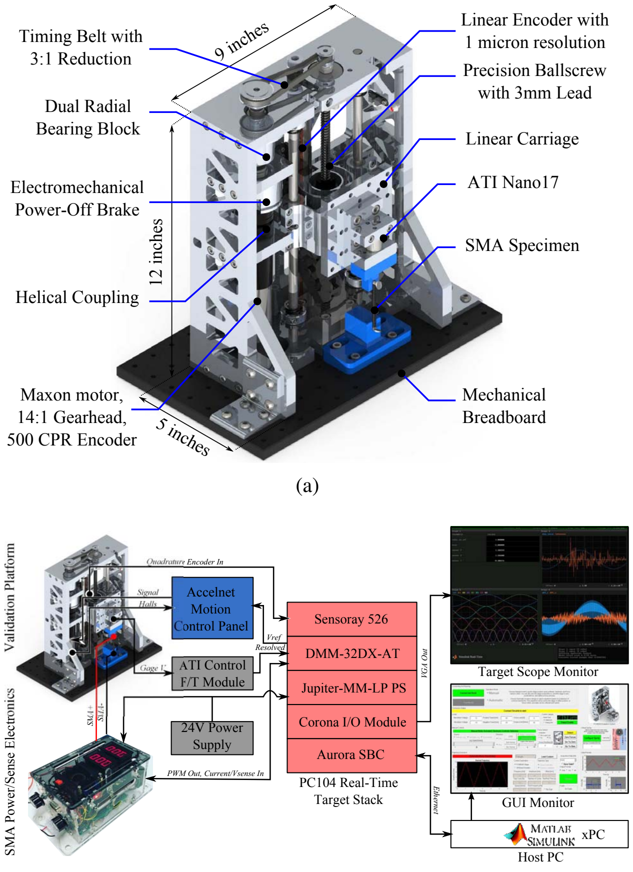

(a)

(b)

Fig. 6. *(a)* Validation platform with callouts to relevant features, *(b)* validation system overview and real-time control architecture.

from the wire leads which is assumed to be negligible. A buck converter allows for precision control of the maximum current available to each SMA. A 5V regulator provides power to two analog current sensors which measure the current through each SMA.

2) Current Control: A low-level PD current controller is implemented based on feedback from each current sensor. Given that the actual sensor output is a square wave due to the PWM drive methodology, we convert this to a variable analog signal by a low-pass filter with a cutoff frequency of 5 Hz to mimic the slow thermomechanical response of the SMA actuator. This filtered signal then drives a PD loop operating at 2 kHz which modulates the duty cycle of the output signal. The controller is implemented in MATLAB xPC and embedded on a PC104 real-time target machine (Diamond Systems Aurora SBC, DMM-32DX-AT Analog/Digital I/O).

IV. VALIDATION

To support actuator characterization efforts, a precision evaluation platform was designed and fabricated to allow for simultaneous SMA current control, execution of position/force-controlled motion profiles, and data logging.

A. Experimental Setup

The experimental setup is shown in Fig. 6. With a design motivated in part by the off-board system developed in [22], the setup features a custom designed validation platform consisting of a moving metrology stage actuated by a preloaded ballscrew drive (Nook Industries) with high-resolution linear encoder (AK Lida 47, Heidenhain, Inc.) feedback. A Maxon EC-Max brushless DC motor with a 14:1 planetary gearhead drives the ballscrew through a custom quasi-back-to-back dual radial bearing system and a timing-belt transmission. A Copley Accelnet ACP-090-09 controller performs the primary-side commutation and closes a lower-level current loop. A PC104 xPC target system (consisting of a Diamond Systems Aurora SBC, Diamond Systems Jupiter-MM-LP power supply, Diamond Systems DMM-32DX-AT DAQ, and Sensoray 526 quadrature decoder) implements the outer position/force control loop (PID with gravity compensation and velocity/acceleration feed-forward) and data acquisition/filtering in real time. The target system also provides two independent 50Hz PWM signals to drive the antagonistic SMA power electronics with the current control discussed earlier. Force feedback is provided via an ATI Nano17 titanium 6-axis force sensor. A Dell Precision 5810 Workstation serves as the host computer and communicates with the target via ethernet.

B. Blocking Force Evolution

To validate the thermomechanical blocking force model given in Equation (13), actuators were clamped into the system and pre-stretched by 100% of their unstretched length (i.e. $\delta_0 = L_0$). Varying step currents were applied, and the resulting force was recorded via the ATI Nano17. Example results for the optimized actuator are shown in Fig. 7. The model adequately predicts the blocking force evolution as a function of time and current. We observe that rise time can be arbitrarily controlled via the application of more current, and the dynamics scale as expected.

C. Net Force vs. Stroke (Antagonism)

To determine net force vs. stroke, actuators were tested in tension in both martensitic and austenitic states by applying a triangular displacement profile and measuring the resulting

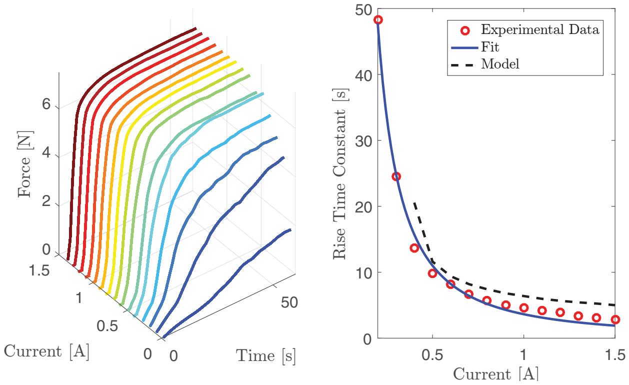

Fig. 7. Blocking force results: *(left)* experimental blocking force vs. time for varying input current, and *(right)* rise time constant vs. input current (experimental vs. theoretical)

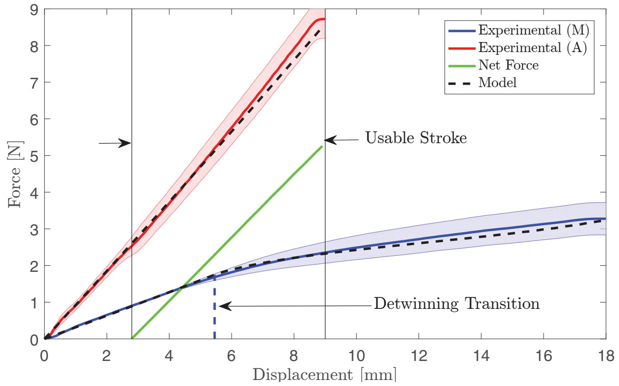

Fig. 8. Antagonism characterization of optimized actuator design, showing a net blocking force of nearly 5.5N at zero strain (or 11N for parallel actuators). The model presented in Section 2 matches the experimental results quite well. The shaded region represents standard deviation over $n = 5$ tests.

force. To simulate antagonism with a pre-stretch of δ_0, austenitic actuators were stretched to a maximum of δ_0 before unloading (to simulate an the actuator contracting from δ_0 to zero). Conversely, martensitic actuators were stretched from zero to $2\delta_0$. Fig. 8 shows the results for the final actuator geometry. By correlating the two curves, we can deduce the net force vs. stroke ($F_{net} = F_{act}(\delta_0 - \delta) - F_{bias}(\delta_0 + \delta)$), and determine the usable stroke by observing the zero-crossing. We see that, for the selected actuator, the antagonistic blocking force is 5.5N (or 11N for actuators in parallel), and the usable stroke is 6 mm. We also observe the benefit of pre-stretching the bias actuator past the detwinning transition stress as the stiffness drops off resulting in greater net force.

D. Forced Cooling

A notable drawback of SMA actuation systems is the fact that the speed of actuation is rate-limited by thermodynamic processes. We demonstrated that it is possible to speed the heat-up time by applying more current. To improve cool-down time, we explore the effects of forced convection in different fluid mediums (air and water) to justify the inclusion of a cooling system for performance enhancement. Actuators were stretched to 100% of their unstretched length, and a current of 1.4A was applied to initiate the austenitic phase transition. After steady-state was reached, the current was removed, and the actuators were allowed to cool under three conditions: (a) free convection with air, (b) forced convection with air (via a computer fan), and (c) forced convection with water (by applying droplets of water via a syringe). The results, shown in Fig. 9, demonstrate that the cooling speed is dramatically improved via forced convection techniques. This experiment validates the inclusion of forced fluidic cooling infrastructures to achieve practical actuation speeds.

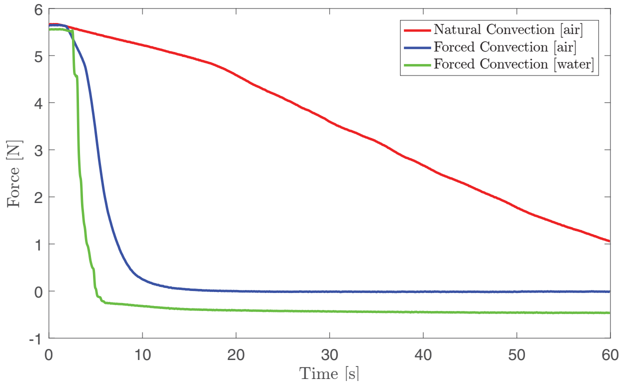

Fig. 9. Effect of different cooling modalities on actuator relaxation. Through forced cooling with a fluid medium, we can improve the cooling time constant from 50 seconds to 1 second.

V. INTEGRATED SYSTEM

To demonstrate practical implementation of the high-force, high-stroke antagonistic actuation scheme, a to-scale robotic module was built to interface with an Olympus CF-100L 13mm endoscope. The module design and preliminary integrated system tests are described below.

A. Module Design

The fabricated module is shown integrated onto the endoscope in Fig. 10(a). An exploded view of the integrated module is shown in Fig. 10(b). The actuator module contains channels for the parallel actuators, as well as in inlet for fluid flow and features for dispersing the flow over the actuators. The actuator module was appropriately sized such that its inclusion does not interfere with the endoscope's built-in degrees of freedom in the interest of system transparency when not in use. The parallel actuators are coupled to the deflection plate via high temperature Kevlar fiber to fully isolate the SMA from the anatomy with the addition of protective covers which snap into the actuator module. A transparent deflector plate is laser-cut from optically clear acrylic and fastened to a pin-joint-based articulating element. The deflection plate features a through-hole that engages with tools passed through the working channel, thereby transmitting forces to the tool to deflect it laterally.

A torque balance about the pin joint as shown in Fig. 10(c) yields the following expression:

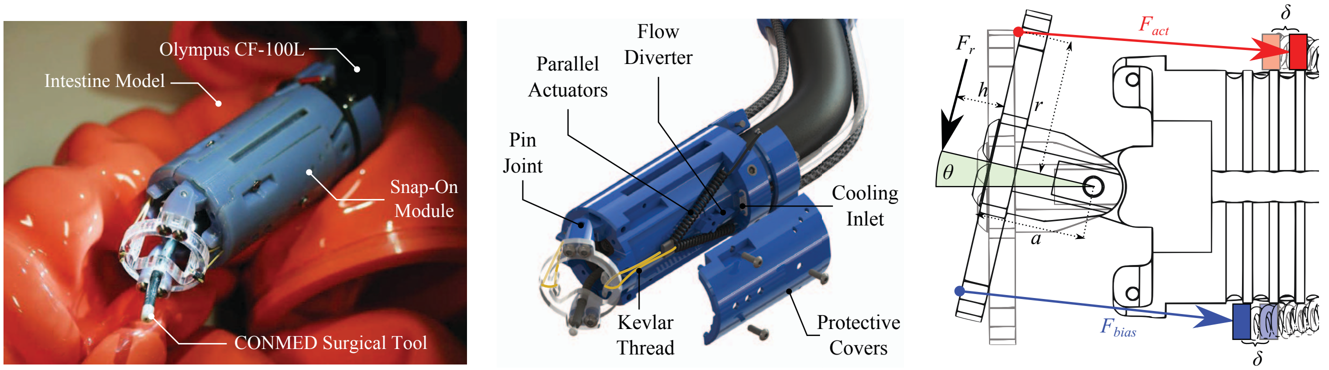

(a) (b) (c)

Fig. 10. *(a)* To-scale prototype integrated onto a 13mm endoscope, passed through an analog of the lower intestine, *(b)* exploded view showing actuator configuration and fluid cooling channels, *(c)* mechanical schematic showing relevant geometric parameters and force balance.

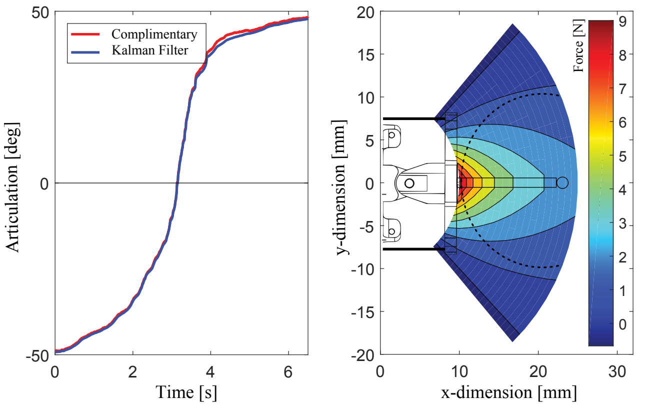

Fig. 11. Workspace analysis: *(left)* full sweep results demonstrating nearly 100 degrees of articulation, *(right)* workspace reconstruction (extrapolated to account for tool stranslation) where contours show the maximum lateral force from Equation (19) and the dotted line indicates a 2cm tumor.

$$F_r = \frac{r}{a+h}(F_{act} - F_{bias})\cos(\theta) \tag{19}$$

where r is the deflection plate radius, and h is the offset distance between the plate and the reaction force F_r.

B. *Workspace Characterization*

To determine the reachable workspace, a 6-axis IMU (MPU6050) was rigidly fixed to the deflector plate, and the system was actuated from negative to positive extreme while angular data was collected along the yaw axis. The results were filtered using both an extended Kalman filter and a complimentary filter (Fig. 11(a)) to show that the system can generate +48/-48 degrees of distal articulation for 96 degrees overall, thereby exceeding our functional requirement of 90 degrees [10]. Fig. 11(b) shows the resulting reachable workspace assuming a rigid transformation between the deflector plate and the tool tip, and the theoretical force profile is computed from Equation (19). As ESD primarily targets lesions with diameters of 2cm and less, and prior studies showed forces on the order of 300-400 mN required to remove tissue during electrosurgery [10], the proposed module is capable of providing the range of articulation and force required to assist the circumferential incision of gastric tumors.

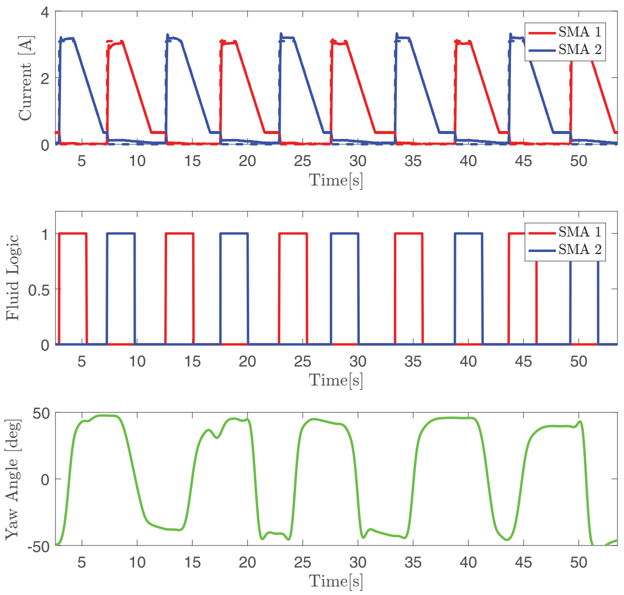

Fig. 12. Open loop control results: *(top)* alternating dynamic current profiles ensure fast heat-up followed by low-current phase sustain (dotted line indicates desired profile, solid line indicates actual profile), *(middle)* fluid logic showing flushing of the bias actuator, *(bottom)* resulting yaw angle.

C. *Open-Loop Control and Demonstration*

An open-loop controller was implemented in MATLAB xPC and embedded on the PC104 system described previously. The controller implements the aforementioned current controller and generates current profiles with high-current transients for fast heat-up which slew to a steady-state low-current to sustain the transition temperature while preventing overheating. Meanwhile, digital logic signals control solenoid valves which provide fluid cooling to the module. This sequence is shown in Fig. 12 along with the resulting yaw angle as measured by the IMU. Observe that fluid cooling allows the system to traverse through its range of motion at

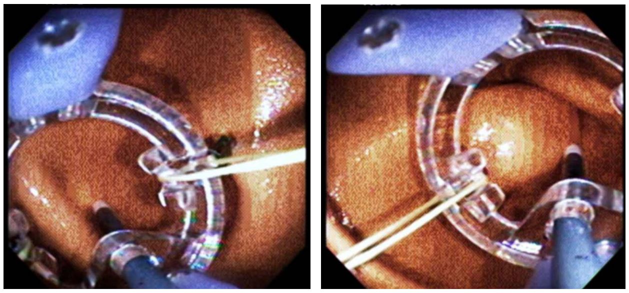

Fig. 13. View through endoscope camera during an actuation cycle, showing the system deflecting a tool to contact tissue.

least 10 times in 55 seconds, in about the same amount of time it would take to switch once without cooling.

The prototype was integrated onto the distal end of an Olympus CF-100L endoscope and passed into the large intestine of a GI simulator (AK107 Lower GI Endoscopy Simulator, Adam-Rouilly). A flexible GI probe (Conmed) was passed through the endoscope and into the deflector cap, and the module was actuated through its range of motion. Images of this process are shown in Fig. 13. The results demonstrate the clarity of the visual field, as the tip of the tool is always visible. In addition, the system generates enough force to deflect the tool, while still allowing axial translation.

VI. CONCLUSION AND FUTURE WORK

In this paper we present a distal robotic module with integrated actuation capable of generating an additional 96 degrees of deflection and sufficient lateral forces for fine control of endoscopic tools. Using a combination of theory and heuristics, we designed an optimum actuator for generating the required force and stroke, and implemented the actuator in a to-scale modular roboendoscopic system. Future work will focus on design for manufacturing such that the components can be molded, as well as proprioceptive sensor implementation to enable closed-loop control for automated trajectory execution using a similar fabrication approach as described in [10]. In addition, we will collaborate with experimental endoscopists to test the device *ex-vivo* on appropriate ESD analogs (pig stomachs) as a stepping stone towards *in-vivo* animal studies on anesthetized pig models.

REFERENCES

[1] K. Taniguchi, A. Nishikawa, and M. Sekimoto, “Classification, design and evaluation of endoscope robots,” *Robot Surgery*, vol. 1, no. January, p. 172, 2010.

[2] Y. Chen, S. Tanaka, and I. W. Hunter, “Disposable endoscope tip actuation design and robotic platform.,” *Conference proceedings : ... Annual International Conference of the IEEE Engineering in Medicine and Biology Society. IEEE Engineering in Medicine and Biology Society. Conference*, vol. 2010, pp. 2279–2282, 2010.

[3] K.-y. Ho, S. J. Phee, A. Shabbir, S. C. Low, V. A. Huynh, A. P. Kencana, K. Yang, D. Lomanto, B. Y. J. So, Y. Y. J. Wong, and S. C. S. Chung, “Endoscopic submucosal dissection of gastric lesions by using a Master and Slave Transluminal Endoscopic Robot (MASTER).,” *Gastrointestinal endoscopy*, vol. 72, no. 3, pp. 593–9, 2010.

[4] G. P. Mylonas, V. Vitiello, T. P. Cundy, A. Darzi, and G.-z. Yang, “CYCLOPS : A Versatile Robotic Tool for Bimanual Single-Access and Natural-Orifice Endoscopic Surgery,” *IEEE International Conference on Robotics and Automation*, pp. 2436–2442, 2014.

[5] J. Ruiter, E. Rozeboom, M. Van Der Voort, M. Bonnema, and I. Broeders, “Design and evaluation of robotic steering of a flexible endoscope,” *Proceedings of the IEEE RAS and EMBS International Conference on Biomedical Robotics and Biomechatronics*, pp. 761–767, 2012.

[6] M. F. Traeger, D. B. Roppenecker, M. R. Leininger, F. Schnoes, and T. C. Lueth, “Design of a spine-inspired kinematic for the guidance of flexible instruments in minimally invasive surgery,” *2014 IEEE/RSJ International Conference on Intelligent Robots and Systems*, no. Iros, pp. 1322–1327, 2014.

[7] A. Arezzo, A. Menciassi, P. Valdastri, G. Ciuti, G. Lucarini, M. Salerno, C. Di Natali, M. Verra, P. Dario, and M. Morino, “Experimental assessment of a novel robotically-driven endoscopic capsule compared to traditional colonoscopy,” *Digestive and Liver Disease*, vol. 45, no. 8, pp. 657–662, 2013.

[8] K. Kume, N. Sakai, and T. Goto, “Development of a novel endoscopic manipulation system : the Endoscopic Operation Robot ver . 3,” *Endoscopy*, vol. 47, pp. 815–819, 2015.

[9] A. Faragasso, A. Stilli, J. Bimbo, Y. Noh, H. Liu, T. Nanayakkara, P. Dasgupta, H. A. Wurdemann, and K. Althoefer, “Endoscopic add-on stiffness probe for real-time soft surface characterisation in MIS,” *Conference proceedings : ... Annual International Conference of the IEEE Engineering in Medicine and Biology Society. IEEE Engineering in Medicine and Biology Society. Annual Conference*, vol. 2014, pp. 6517–6520, 2014.

[10] J. Gafford, T. Ranzani, S. Russo, H. Aihara, C. Thompson, R. Wood, and C. Walsh, “Snap-on robotic wrist module for enhanced dexterity in endoscopic surgery,” *2016 IEEE International Conference on Robotics and Automation (ICRA)*, pp. 4398–4405, 2016.

[11] J. B. Gafford, R. J. Wood, and C. J. Walsh, “Self-Assembling, Low-Cost, and Modular mm-Scale Force Sensor,” *IEEE Sensors Journal*, vol. 16, no. 1, pp. 69–76, 2016.

[12] J. Gafford, F. Doshi-Velez, R. Wood, and C. Walsh, “Machine learning approaches to environmental disturbance rejection in multi-axis optoelectronic force sensors,” *Sensors and Actuators A: Physical*, vol. 248, pp. 78–87, 2016.

[13] M. Ho, A. B. McMillan, J. M. Simard, R. Gullapalli, and J. P. Desai, “Toward a meso-scale SMA-actuated MRI-compatible neurosurgical robot,” *IEEE Transactions on Robotics*, vol. 28, no. 1, pp. 213–222, 2012.

[14] Z. Y. Shi, D. Liu, and T. M. Wang, “A shape memory alloy-actuated surgical instrument with compact volume,” *Int J Med Robotics Comput Assist Surg*, vol. 2000, no. October 2013, pp. 474–481, 2014.

[15] N. Pappafotis, W. Bejgerowski, R. Gullapalli, J. M. Simard, S. K. Gupta, and J. P. Desai, “Towards Design And Fabrication Of A Miniature Mri-Compatible Robot For Applications In Neurosurgery,” *Detc 2008: 32nd Annual Mechanisms And Robotics Conference, Vol. 2, Pts A & B*, no. August, pp. 747–754, 2009.

[16] J. Szewczyk, V. de Sars, P. Bidaud, and G. Dumont, *An active tubular polyarticulated micro-system for flexible endoscope*, pp. 179–188. Berlin, Heidelberg: Springer Berlin Heidelberg, 2001.

[17] M. Ho, S. Member, J. P. Desai, and S. Member, “Modeling , Characterization and Control of Antagonistic SMA Springs for use in a Neurosurgical Robot,” in *Robotics and Automation (ICRA), 2013 IEEE International Conference on*, (Karlsruhe, Germany), pp. 2503–2508, 2013.

[18] C. Liang and C. A. Rogers, “A multi-dimensional constitutive model for shape memory alloys,” *Journal of Engineering Mathematics*, vol. 26, no. 3, pp. 429–443, 1992.

[19] Y. Toi, J.-b. Lee, and M. Taya, “Finite element analysis of superelastic , large deformation behavior of shape memory alloy helical springs,” *Computers and Structures*, vol. 82, pp. 1685–1693, 2004.

[20] L. Brinson, “One-Dimensional Constitutive Behavior of Shape Memory Alloys: Thermomechanical Derivation with Non-Constant Material Functions and Redefined Martensite Internal Variable,” *Journal of Intelligent Material Systems and Structures*, vol. 4, pp. 229–242, 1993.

[21] S.-m. An, J. Ryu, M. Cho, and K.-j. Cho, “Engineering design framework for a shape memory alloy coil spring actuator using a static two-state model,” *Smart Materials and Structures*, vol. 21, pp. 1–16, 2012.

[22] Y. Ding, I. Galiana, A. Asbeck, B. Quinlivan, S. M. M. D. Rossi, and C. Walsh, “Multi-joint actuation platform for lower extremity soft exosuits,” in *2014 IEEE International Conference on Robotics and Automation (ICRA)*, pp. 1327–1334, May 2014.